



Microwave synthesized complex concentrated alloy coatings: Plausible solution to cavitation induced erosion-corrosion

Rakesh B. Nair, H.S. Arora, H.S. Grewal*

Surface Science and Tribology Lab, Department of Mechanical Engineering, Shiv Nadar University, Gautam Budh Nagar, India



ARTICLE INFO

Keywords:

Cavitation erosion-corrosion
Complex concentrated alloys
Microwave processing
Electrochemical corrosion
Strain-hardening

ABSTRACT

Surface phenomenon such as cavitation erosion-corrosion limits the working life and durability of the fluid machines through significantly altering the efficiency. Surface modification is an apparent and economical route for improving the sustainability of these components. Recently developed complex concentrated alloys (CCAs) or high entropy alloys (HEAs) possess exceptional properties owing to high configurational entropy. We developed CCA coatings on the stainless steel using a facile and effective microwave processing technique. The effect of Al molar fraction in $Al_xCoCrFeNi$ ($x = 0.1-3$) CCAs on ultrasonic cavitation erosion-corrosion was investigated in 3.5% NaCl solution. For comparison, cavitation erosion and electrochemical corrosion behavior of the pre- and post-tested samples was also performed. Detailed microstructure and mechanical characterization of the developed coatings were also performed using different analytical techniques. The equimolar CCA coating showed apical degradation resistance under both pure erosion and erosion-corrosion conditions. The observed behavior is attributed to high strain hardening, optimal hardness, fracture toughness, and utmost stability of the passive layer. The phenomenal conjugation of these properties was associated with highest configurational entropy for equimolar composition resulting in sluggish diffusion, and severe lattice straining. Compared to pits, striations and cracks characterizing the morphology of the degraded stainless steel, the equimolar and $Al_{0.1}CoCrFeNi$ CCAs showed TTS (tearing topograph surface) as the dominant failure mode characterized by presence of microplastic deformation. The degradation of the $Al_3CoCrFeNi$ CCA occurred mainly through brittle failure mode. The difference in failure mechanism is related to the mechanical properties and underlying microstructure.

1. Introduction

The performance of different fluid machines and associated components such as turbines, pumps, impeller, control valves, and pipes is severely affected due to cavitation erosion. The sustainability of these systems is profoundly impaired owing to an increase in downtimes, and repairs, contributing to the operational cost. Cavitation erosion is a complex phenomenon originating from pressure fluctuations inside the flow field resulting in formation and implosion of vapor bubbles [1]. Imploded bubbles result in high velocity micro-jets and shockwaves, damaging adjacent solid surfaces. Repeated impact of these micro-jets and shockwave at a high frequency emanates fatigue damages of materials [1,2]. The presence of corrosive media further aggravates the damaging process due to synergistic effect between cavitation erosion (mechanical action) and corrosion (electrochemical action). The repeated implosion of vapor bubbles damages protective passive film, accelerating corrosion process. Recent investigation indicates the cost of tribo-corrosion to be around 3.4% of the GDP in developed countries

[3]. Thus, effective solutions are required to improve durability of the components working under extreme conditions and control the rising operating costs. This demands development of advanced materials to combat the deleterious effects of tribo-corrosion. Subsequently, coatings provide an eminent and cost-effective solution compared to bulk counterparts.

Recently emerged, complex concentrated alloys (CCAs) or high entropy alloys (HEAs) represent a new realm of metallic alloys composed of multi principal elements compared to conventional alloy design strategies. CCAs are composed of equimolar/nearly-equimolar concentrations with atomic fractions varying within 5–35% [4,5]. Owing to large configurational entropy, the systems stabilize to form a single phase solid solution due to reduced Gibbs free energy. The developed material systems stabilize to form simple lattice structures such as face centered cubic (FCC), body centered cubic (BCC), and hexagonal closed packed (HCP) or their combinations owing to high configurational entropy [6]. Further, the compositional complexity of CCAs enhances the lattice distortion and lowers the diffusion kinetics by

* Corresponding author.

E-mail addresses: harpreetsg@iitrpr.ac.in, harpreet.grewal@snu.edu.in (H.S. Grewal).

<https://doi.org/10.1016/j.ultsonch.2018.09.004>

Received 31 March 2018; Received in revised form 30 August 2018; Accepted 2 September 2018

Available online 03 September 2018

1350-4177/ © 2018 Elsevier B.V. All rights reserved.

trapping atoms at lower potential energy (LPE) sites. The interactions among the constituent elements also contribute to the exceptional properties observed for CCAs (cock tail effect) [6]. Owing to these core effects, CCAs are reported to have excellent properties such as high temperature strength and hardness, high ductility, superior wear resistance, exceptional corrosion and oxidation resistance [7–11].

Although limited, few studies have explored the cavitation erosion and corrosion behavior of complex concentrated alloys. Laser surface alloyed AlCoCrFeNi CCA showed enhanced cavitation erosion and corrosion resistance compared to stainless steel due to the presence of BCC phase [12]. Wu et al. [13] reported an increase in cavitation erosion resistance of AlCoCrFeNiTi_x CCA as a function of Ti content, which is attributed to the presence of intermetallic phases. Our recent study also showed excellent cavitation erosion-corrosion resistance of Al_{0.1}CoCrFeNi CCA compared to SS316L steel [7]. Few studies also investigated the standalone electrochemical corrosion behavior of the CCAs [10,14–16]. For Al_xCoCrFeNi CCAs, the corrosion behavior has been observed to exhibit inverse relation with the Al content due to the presence of Cr depleted region resulting from segregation of Al-Ni rich phase in the dendritic region [10]. On the other hand, hardness and strength showed direct correlation with Al content for Al_xCoCrFeNi CCAs. Evaluating the performance of Al_xCoCrFeNi CCAs under tribo-corrosion conditions as a function of Al is required for better understanding of the structure-property relation of the CCAs.

Cavitation erosion-corrosion being a surface phenomenon, various coating approaches have been hypothesized in order to control its nocuous effects [17–19]. However, coatings synthesized using these conventional techniques suffer from inherently derived microstructural defects such as pores and splat boundaries in case of thermal spraying. Further, need of controlled environment and low deposition rates have limited the usability of physical and chemical vapor deposition techniques. Microwave hybrid processing (MHP) is an imminent and feasible method for developing coatings due to its unique volumetric heating characteristic. Microwave processing comprises of rapidly heating the material owing to direct coupling with electromagnetic energy [20]. Previous studies related to the synthesis of CCAs using microwave technique has been limited to evaluation of the microstructural aspects and mechanical properties [21,22]. Colombini et al [23] studied the microwave technique to synthesize AlCoCrFeNi CCA using different processing routes. Veronesi et al [24] synthesized Mn₂₅Fe_xNi₂₅Cu_(50-x) HEA with Si addition using microwave heating. Small needle structures with Cu-rich interdendrites were formed due to its positive mixing enthalpy.

In the present work, we report on the development of Al_xCoCrFeNi (x = 0.1–3) CCA coatings using MHP technique. The effect of Al content on microstructure and different mechanical properties was investigated. Performance of the developed CCA coatings under combined and standalone ultrasonic cavitation erosion and corrosion environments was evaluated in comparison with SS316L substrate steel. Correlation with different mechanical properties was attempted to develop further understanding of significant physical properties controlling the degradation behavior of CCAs. Post testing analysis of the samples was performed to identify the material removal mechanism and role of passive layer in synergistic environment.

2. Experimental

2.1. Coating preparation

Complex concentrated alloy (CCA) precursor powders with different elemental compositions (Table 1) were deposited on SS316L stainless steel substrate. The microstructure of the Al_xCoCrFeNi CCA system can be modulated as a function of Al fraction and forms a basis for understanding the structure-property correlations in case of CCAs. Three coating compositions were prepared by varying Al fraction (x = 0.1–3). High purity (99.9%) elemental feedstock powders were used for

Table 1

Nominal composition of Al_xCoCrFeNi complex concentrated alloys in wt.% for developing coatings using microwave processing technique.

Coatings	Al	Cr	Co	Fe	Ni
Al _{0.1} CrCoFeNi	1.2	22.8	25.8	24.5	25.7
AlCrCoFeNi	10.8	20.5	23.4	22.1	23.2
Al ₃ CrCoFeNi	26.4	17.1	19.2	18.2	19.1

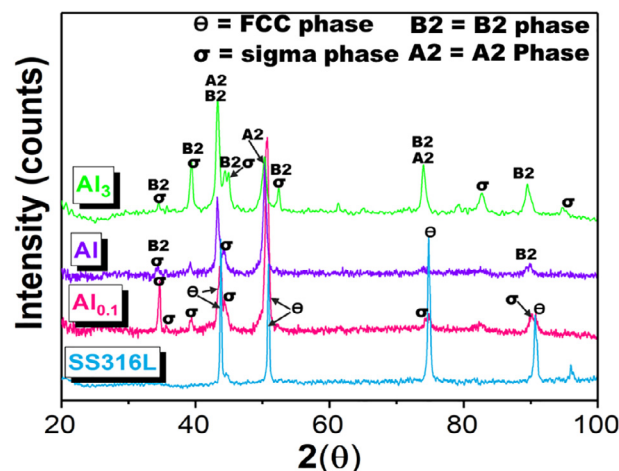


Fig. 1. X-ray diffraction (XRD) patterns of microwave derived Al_xCoCrFeNi (x = 0.1–3) complex concentrated coatings.

deposition of the coatings. Prior to deposition, the precursor powders were pulverized for 30 mins to ensure homogeneity. Commercially available stainless steel SS316L were machined to 10 × 10 × 5 mm³ size and used as substrate. Prepared specimens were ultrasonically cleaned using acetone followed by drying in air. Precursor powders were spread on the substrate and kept inside the alumina crucible which allows direct interaction of coating powder and susceptor with microwave irradiation. Coating time (8 min) and power (900 W) were optimized through several hit-and-trial runs. Detailed description of coating development has been reported elsewhere [25]. Charcoal was used as a susceptor material due to its high loss tangent value. The precursor powder couples with microwaves beyond a threshold temperature resulting in volumetric heating. This results in a high heating rate measured to be around 3.2 °C/s compared to the conventional heating technique observed to 5–20 °C/min. Thus, a combined conductive heating of coating material by susceptor and volumetric heating of powders results in a hybrid heating mode.

2.2. Microstructural and mechanical characterizations

All the coated samples were sectioned along the cross-section using low speed diamond saw for the microstructural and mechanical characterization. Prior to analysis the samples were polished and ground down to 3000 grit followed by final polishing using 0.1 μm diamond paste and cleaned with acetone. X-ray diffraction (XRD) (Bruker, D8 Discover) analysis was performed for all the coatings using Cu- α radiation ($\lambda = 1.54 \text{ \AA}$) with a scan rate of 0.02 deg/min. The optical microscope (Leica, DM 750M) and scanning electron microscope (SEM) equipped with energy dispersive spectroscopy (EDAX) (Carl ZEISS, EVO 18, Germany) were used to examine the microstructure of the developed CCA coatings. Mechanical characterization of the coatings and substrate was performed using micro- and nano-indentation testings. Microhardness testing (Wilson, MV 402D) was conducted on the cross-sectioned samples using Vickers indenter at a normal load of 50gf with 10 sec dwell time. Nano-indentation test (Hystriion, TI950) was performed to evaluate the elastic modulus, and strain hardening exponent

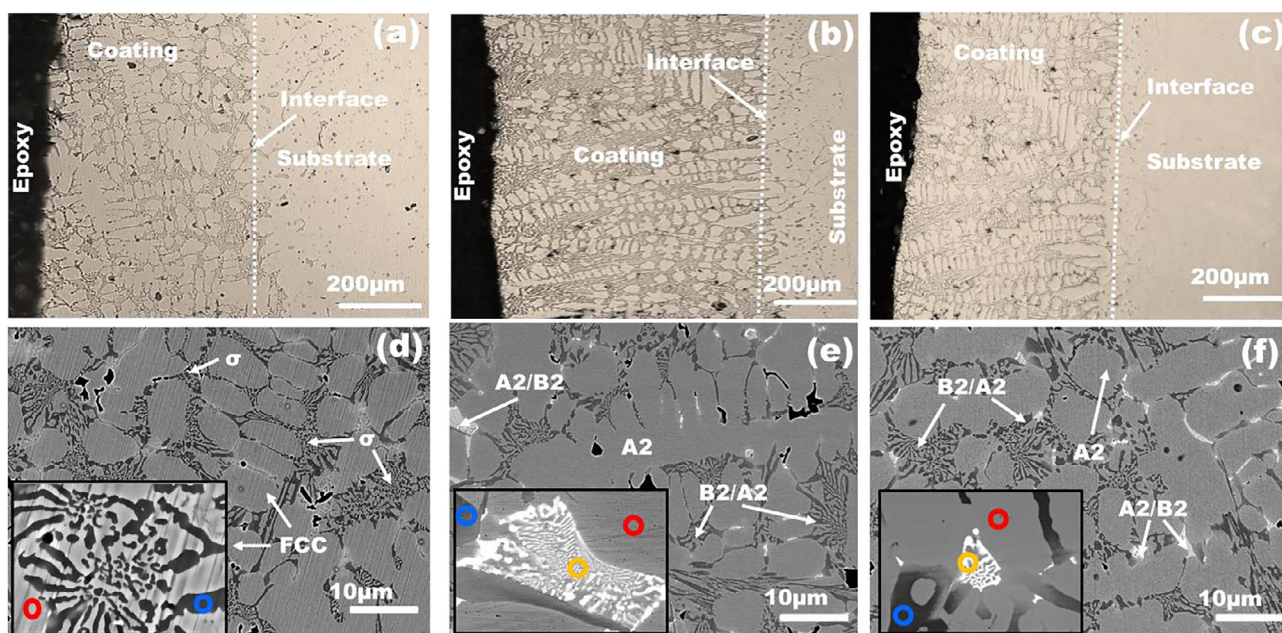


Fig. 2. (a-c) Optical and (d-f) scanning electron microscope image showing microstructure of the (a) and (d) $\text{Al}_{0.1}\text{CoCrFeNi}$, (b) and (e) AlCoCrFeNi and (c) and (f) coatings synthesized using microwave processing [25]. Insets show high magnification images of different phases. The composition of the phases is highlighted using different symbols and presented in Table 2.

Table 2

Energy dispersive spectroscopy results for the $\text{Al}_x\text{CoCrFeNi}$ complex concentrated coatings deposited on the SS316L stainless steel substrate using microwave processing technique [25].

Composition $\text{Al}_x\text{CoCrFeNi}$	Region	Elements are in at. %					
		Al	Co	Cr	Fe	Ni	Mo
x = 0.1	● Intracellular	2.9	19.4	19.1	28.2	26.2	4.2
	● Intercellular (grey)	1.8	27.6	25	18	16	11.6
x = 1.0	● Intracellular	12.6	22.2	21.3	21.2	11.2	11.5
	● Intercellular (grey)	25.2	9.4	14.3	25.4	22.3	3.4
	● Intercellular (white)	15.3	19.6	21.8	16.5	16.4	10.4
x = 3.0	● Intracellular	34.2	16	15.2	14.4	10.5	9.7
	● Intercellular (grey)	42.2	11.1	8.4	15.2	17.6	5.5
	● Intercellular (white)	27.5	14.7	18.4	14.5	13.7	11.2

(n). Elastic modulus was calculated using Oliver-Phar method from the slope of unloading curves [26]. Fracture toughness was evaluated using micro-indentation technique using Lawn, Marshal and Evans equation at a load of 1 kgf using Vickers indenter [27].

2.3. Cavitation erosion-corrosion test

The cavitation erosion-corrosion testing was conducted using ultrasonic vibratory apparatus in accordance to ASTM G32 standard [28]. A detailed description of the set-up is provided elsewhere [7]. The coated samples were held stationary below the vibrating tip (indirect method) at a distance of 500 μm . The frequency of vibrating tip was 20 ± 0.5 kHz with peak-to-peak amplitude of 50 μm . Test samples were submerged in one litre distilled water for pure erosion studies and in 3.5% NaCl solution for erosion-corrosion studies. The temperature

was kept constant at $24 \pm 2^\circ\text{C}$ using chilling unit. Prior to cavitation studies, each sample (10 \times 10 mm) was ground down to 3000 grit using emery paper, ultrasonically cleaned and dried. As-received SS316L stainless steel was used as a reference material and tested under similar conditions. All samples were tested for total of 20 h with subsequent change in mass (0.01 mg) monitored after every one-hour cycle. Two samples of each type were tested under each test condition to ensure repeatability. The obtained results were analysed to calculate cumulative volume loss (CVL), cumulative volume removal rate (CVR), mean depth erosion rate (MDER) and incubation period (IP) for both erosion and erosion-corrosion conditions. The morphology of eroded surfaces was analysed using scanning electron microscope (SEM) to investigate the damage mechanism.

2.4. Electrochemical corrosion test

Electrochemical corrosion tests (Gamry, 1000E) were performed for the coated and uncoated stainless steel samples using a standard three electrode cell configuration with graphite rod as a counter electrode (CE), saturated calomel electrode (SCE) as a reference electrode (RE) and sample as a working electrode (WE). Tafel tests were conducted in the voltage range of -0.4 V to 0.4 V vs open circuit potential (E_{OCP}) with the scan rate of 0.166 mV/s. Electrochemical impedance spectroscopy (EIS) test was also performed with a frequency range of 10^{-2} Hz to 10^5 Hz with a current voltage amplitude of 10 mV. Two replicas were tested for each sample and the average values are reported for both test.

3. Results and discussions

3.1. Microstructural evaluation

The XRD patterns of CCA coated samples are shown in Fig. 1. Phase transformation from FCC ($\text{Al}_{0.1}\text{CoCrFeNi}$) to BCC (AlCoCrFeNi and $\text{Al}_3\text{CoCrFeNi}$) was observed with an increase in Al fraction in accordance with prior studies [29,30]. The $\text{Al}_{0.1}\text{CoCrFeNi}$ alloy showed FCC structure along with the presence of σ phase. For AlCoCrFeNi and $\text{Al}_3\text{CoCrFeNi}$ CCAs ordered (B2) and disordered (A2) BCC phases were observed due to p-d bonding ability of Al with transition elements. The

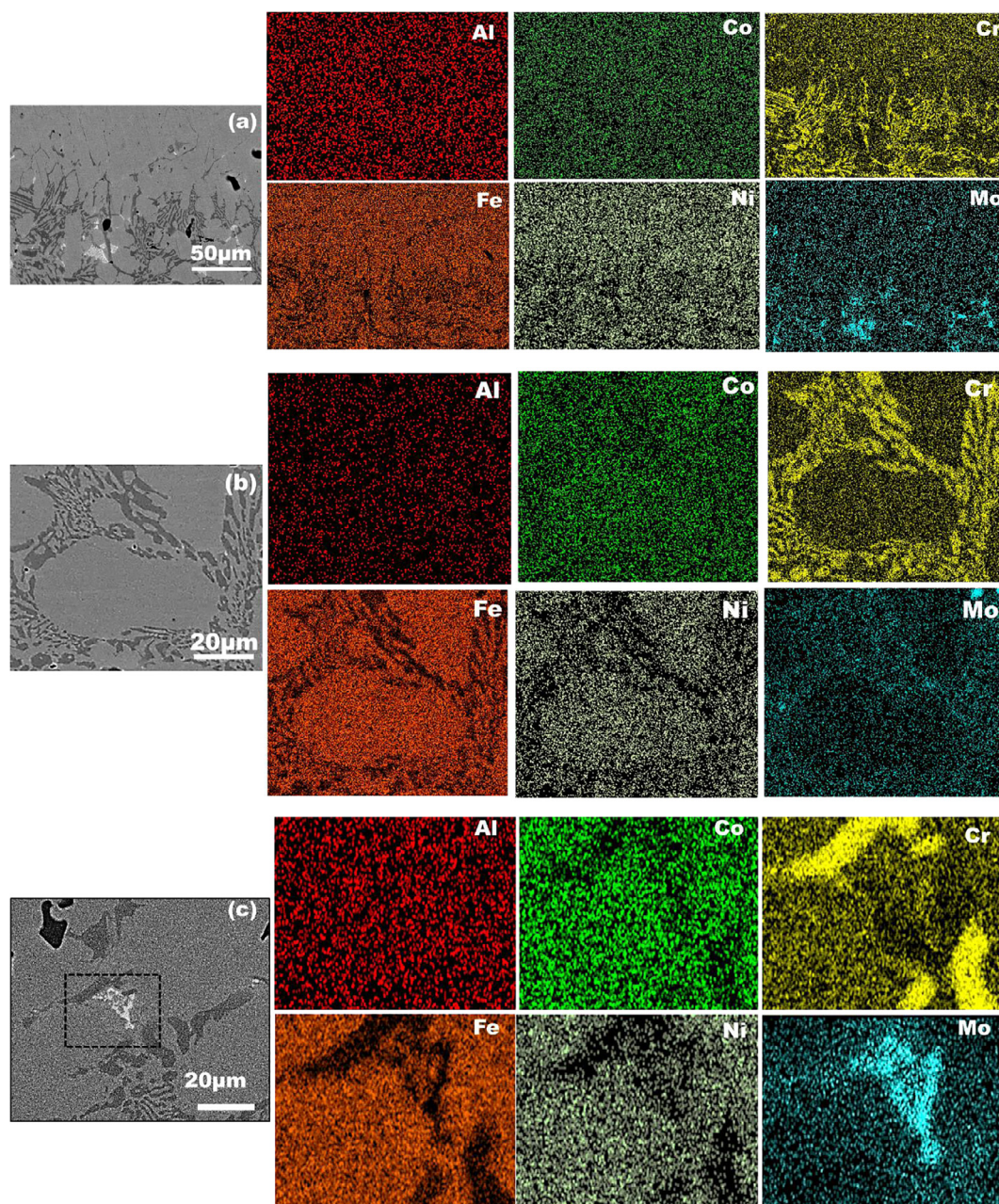


Fig. 3. Energy dispersive spectroscopy (EDAX) area maps showing the elemental distribution at the (a) interface of the coating and substrate (b) intercellular and intracellular region of $\text{Al}_{0.1}\text{CoCrFeNi}$ (c) Cr- and Mo-rich phases formed in AlCoCrFeNi coating.

p-d bonding refers to lateral overlap bonding of p-orbital of Al with those of the d-orbital of the transition elements. The intermetallic σ phase results from the tetragonal arrangement of the atoms while, the B2 phase is the ordered BCC structure wherein the body center position is occupied by the atom type different from that present at the corner positions [6]. Both these phases are hard and brittle in nature. Optical micrographs (OM) and SEM images showing the evolved microstructure of the coatings are shown in Fig. 2. The cellular structure with a size (~ 27 to $33 \mu\text{m}$) and average coating thickness of around 550 – $600 \mu\text{m}$ was observed for all coated samples. Coatings showed lower porosity ($< 1\%$) with diffused interface and without any interfacial cracking (Fig. 2(a) to (c)). Diffused interface obtained for the coatings using microwave processing results in high adhesion with the substrate. The chemical composition of different phases in the coatings (Fig. 2(d) to (f)) evaluated using point EDAX are presented in Table 2. Further, EDAX maps of selected regions are shown in Fig. 3. Fig. 3(a) shows

gradual transition in the elemental concentrations from the substrate to the coating along with diffusion of the Mo to the coating. The intracellular region (red circle) of $\text{Al}_{0.1}\text{CoCrFeNi}$ coating showed a high concentration of Co, Cr, Ni and Fe along with a small concentration of Mo diffused from the substrate (Table 2). Al and Co also diffused into the substrate along the interface. Comparatively, the grey intercellular region (blue circle) of $\text{Al}_{0.1}\text{CoCrFeNi}$ coating showed a high concentration of Cr, Mo, and Co indicating the presence of σ phase as also highlighted by XRD results (Fig. 1). The Mo and Cr are known to promote σ phase formation in the presence of Co and Ni resulting in observed phase evolution [11,31]. Furthermore, the intracellular regions (red circle) of equimolar and three molar Al coatings essentially showed the presence of all elements along with the Mo diffused from substrate (Fig. 3(c)) which in accordance with the XRD results indicates the presence of BCC (A2) phase. The analysis of the grey intercellular region (blue circle) of AlCoCrFeNi and $\text{Al}_3\text{CoCrFeNi}$ showed B2 phase

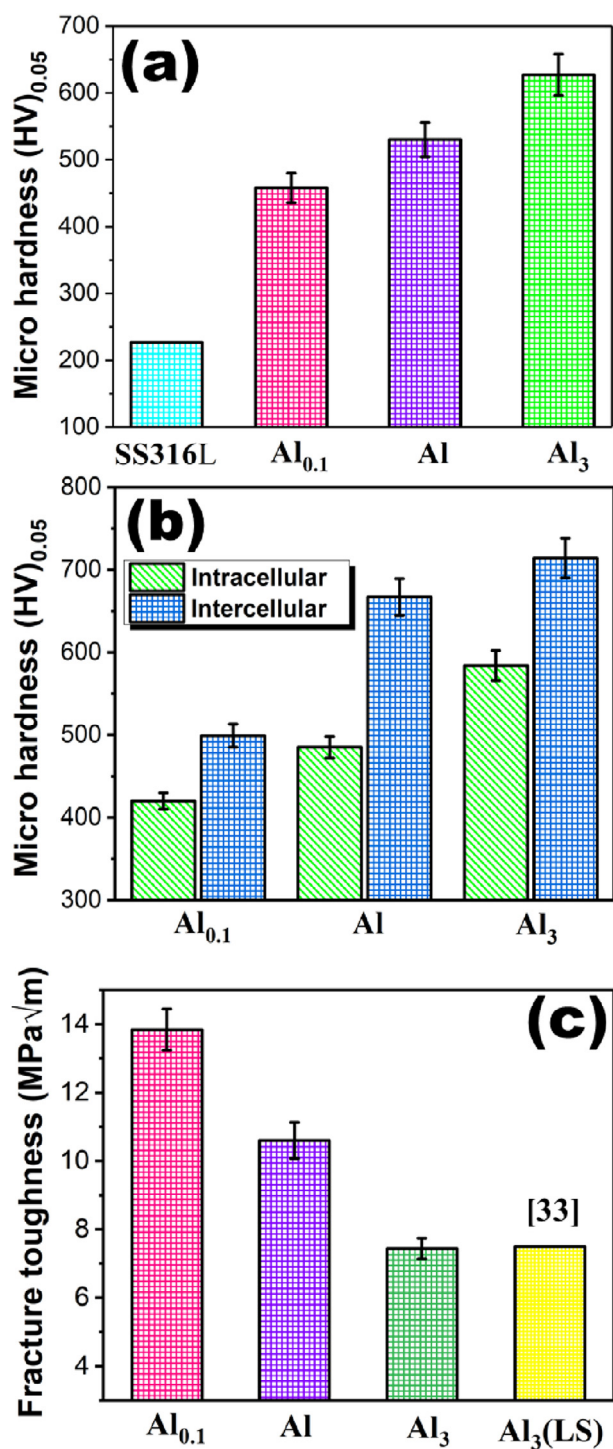


Fig. 4. (a) Average hardness, (b) Hardness of intracellular and intercellular region, (c) Fracture toughness of Al_{0.1}CoCrFeNi, AlCoCrFeNi and Al₃CoCrFeNi complex concentrated coatings synthesized using microwave processing.

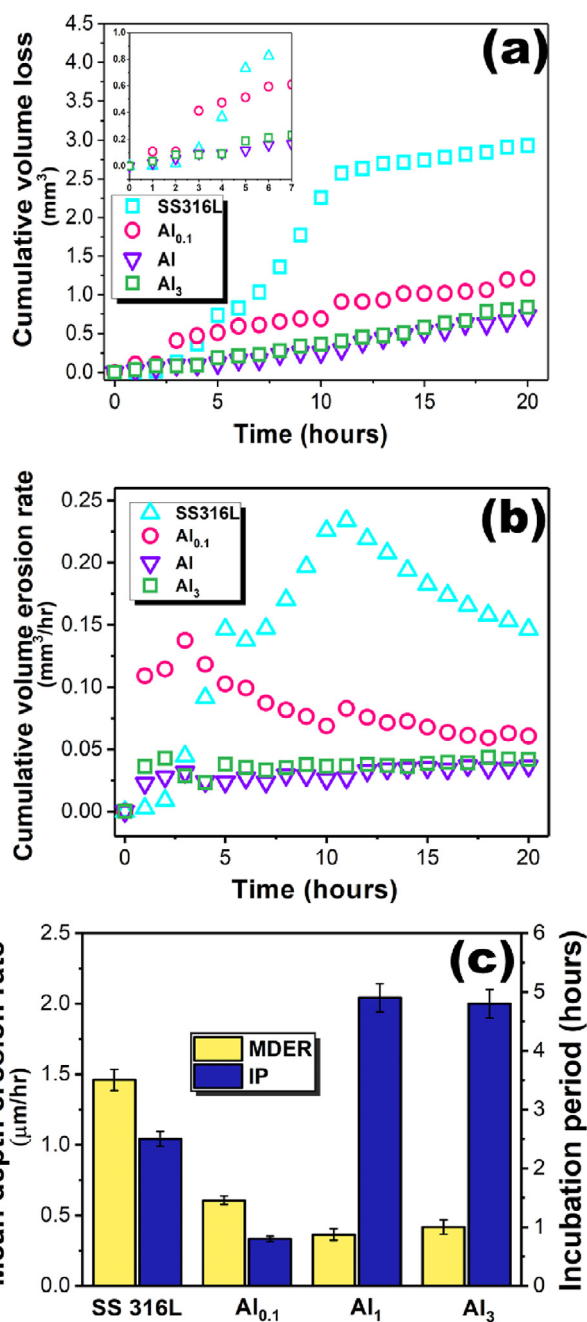


Fig. 5. (a) Cumulative volume loss, (b) cumulative erosion rate as a function of exposure time and (c) mean depth erosion rate and incubation period of Al_{0.1}CoCrFeNi, AlCoCrFeNi and Al₃CoCrFeNi complex concentrated coatings and conventionally used stainless steel 316L subjected to cavitation erosion. Inset in (a) shows the magnified view of the results during initial time period.

embedded in A2 phase. This is also in agreement with the XRD results (Fig. 1). The formation of the B2 phase in the case of AlCoCrFeNi and Al₃CoCrFeNi is promoted by the increased Al content which has large negative mixing enthalpy with many of the constituent elements.

Table 3

Physical and mechanical properties of the microwave synthesized Al_xCoCrFeNi (x = 0.1–3) complex concentrated coatings.

Coatings	Average hardness, H (HV)	Reduced elastic modulus, E (GPa)	Fracture toughness, K _c (MPa.m ^{1/2})	H/E	Density (g/cc)	Strain hardening exponent (n)
Al _{0.1}	458 ± 23	207 ± 5.5	13.84 ± 0.6	0.0217	7.70	0.56
Al	530 ± 31	213 ± 6.2	10.6 ± 0.4	0.0244	6.59	0.62
Al ₃	624 ± 33	192 ± 5.2	7.44 ± 0.3	0.0320	5.26	0.55

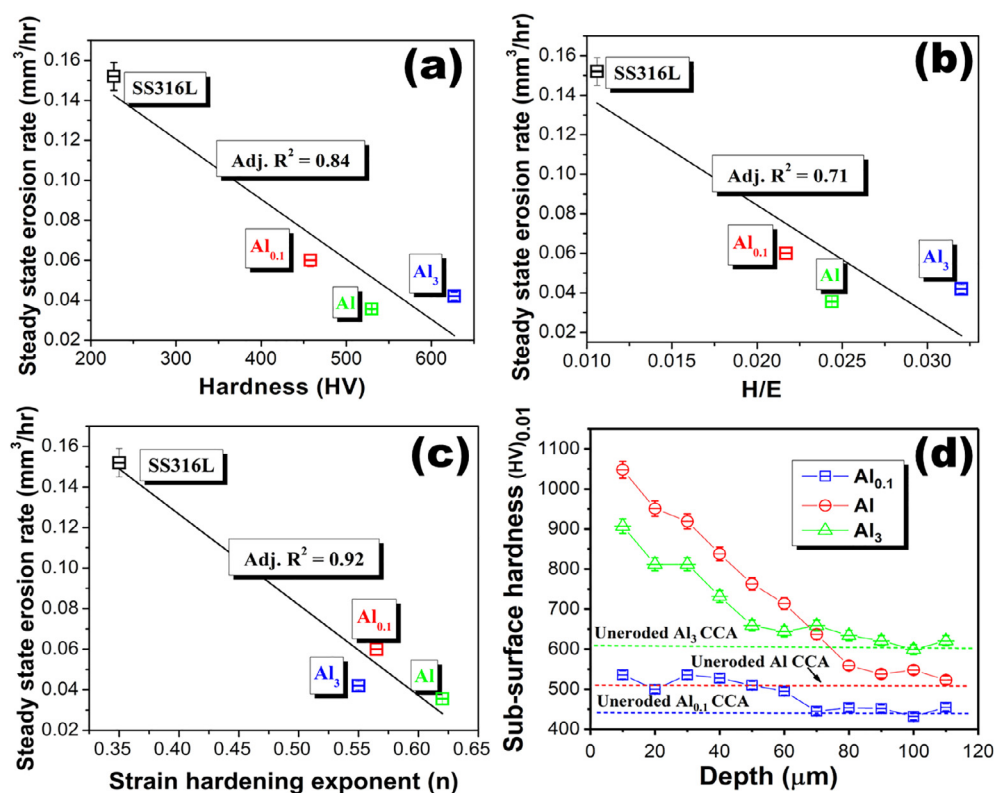


Fig. 6. The correlation of cavitation erosion rate of $\text{Al}_{0.1}\text{CoCrFeNi}$, AlCoCrFeNi and $\text{Al}_3\text{CoCrFeNi}$ complex concentrated coatings and stainless steel 316L with (a) hardness, (b) hardness to modulus ratio (c) strain hardening exponent (n) and (d) shows variation in sub-surface microhardness of the microwave derived $\text{Al}_{0.1}\text{CoCrFeNi}$, AlCoCrFeNi and $\text{Al}_3\text{CoCrFeNi}$ complex concentrated coatings under pure erosion.

Further the white intercellular region (yellow circle) observed for both AlCoCrFeNi and $\text{Al}_3\text{CoCrFeNi}$ coating (Fig. 2(e) and (f)) was rich in Mo, Co, and Cr suggesting A2 embedded in B2 phase. Similar results have been reported previously [32] for the $\text{Al}_x\text{CoCrFeNiMo}_{0.5}$ CCAs developed using arc melting process indicating the efficacy of microwave process in comparison to conventional manufacturing processes based upon lower energy consumption.

3.2. Mechanical characterization

Fig. 4a shows an average hardness for all the CCA coatings measured along the cross-section. Further, the average hardness of intracellular and intercellular regions is also shown in Fig. 4b. Summary of the different mechanical properties obtained for the coatings is listed in Table 3. The $\text{Al}_3\text{CoCrFeNi}$ exhibited highest hardness of 636 HV corresponding to 227 HV observed for the SS316L steel, indicating a three-fold increment. A detailed analysis of the results shows that the hardness of the coatings increases directly with an increase in Al content (Fig. 4a). This result is in accordance with the previous bulk studies [30]. The increased hardness with the addition of Al can be explained on the basis of phase transition from FCC to BCC, formation of hard intermetallic phase and dislocation pinning by a larger sized Al atom. The intercellular region comprised of intermetallic phases (σ and B2) showed extremely high hardness compared with intracellular region (Fig. 4b). High Al fraction results aggravate the dislocation pinning effect and increases the fraction of B2 phase resulting in highest hardness for $\text{Al}_3\text{CoCrFeNi}$. The area fraction of intercellular region was higher for $\text{Al}_3\text{CoCrFeNi}$ (~21.5%) compared to equimolar composition (~18%).

Contrarily, the fracture toughness showed an inverse correlation with Al fraction (Fig. 4c). Higher fracture toughness of $13.8 \text{ MPa}\cdot\text{m}^{1/2}$ was observed for $\text{Al}_{0.1}\text{CoCrFeNi}$ coating while $\text{Al}_3\text{CoCrFeNi}$ showed the lowest value ($7.44 \text{ MPa}\cdot\text{m}^{1/2}$). The fracture toughness observed for microwave processed $\text{Al}_3\text{CoCrFeNi}$ coating was similar to that developed using laser processing ($\sim 7.6 \text{ MPa}\cdot\text{m}^{1/2}$) [33]. Lower fracture toughness for $\text{Al}_3\text{CoCrFeNi}$ coating can also be attributed to a higher

fraction of hard and brittle B2 phase. The $\text{Al}_{0.1}\text{CoCrFeNi}$ coating composed of FCC structure with lower fraction of intermetallic phase showed the highest fracture toughness. The strain hardening exponents (n) calculated using the methodology proposed by Giannakopoulos and Suresh [34] are summarized in Table 3. The value of n was highest for equimolar composition coating compared to non-equimolar composition coatings. Previous study also showed high strain hardening exponent for the $\text{Al}_{0.1}\text{CoCrFeNi}$ CCA bulk [7]. High strain-hardening of the material is generally associated with the low stacking fault energy of the material. The stacking fault energy of the CCAs has been observed to be lower compared to conventional alloys [7,35], resulting in high strain-hardening.

3.3. Ultrasonic cavitation erosion studies

The cumulative volume loss (CVL) and volume removal rates (CVR) as the function of time for all CCA coated samples under cavitation erosion condition are shown in Fig. 5(a) and (b). Results for conventionally used stainless steel 316L tested under similar condition are also shown for reference. The mean depth erosion rate (MDER) and incubation period (IP) are shown in Fig. 5(c). Incubation period (IP) is referred to as minimum time period required to obtain the noticeable volume loss which in our case was 0.1 mm^3 . Prior to the IP, significant plastic deformation occurs without any apparent mass loss. All the coatings show superior cavitation erosion resistance compared to stainless steel after 20 h of testing. After a short incubation period (2.7 h), a sharp increase in CVL and CVR was observed for stainless steel while no significant change was observed for the coated samples except $\text{Al}_{0.1}\text{CoCrFeNi}$. The AlCoCrFeNi and $\text{Al}_3\text{CoCrFeNi}$ alloys show almost similar IP with value around two times higher compared to the stainless steel. High IP is ascribed to lower deformation incurred in the early stage. The $\text{Al}_{0.1}\text{CoCrFeNi}$ showed least incubation period (Fig. 5c) which could be explained on the basis of lower average hardness compared to two other CCA coatings. The maximum erosion rate observed for the stainless steel ($0.233 \text{ mm}^3/\text{h}$) was much higher than that observed for the coatings ($\sim 0.025\text{--}0.14 \text{ mm}^3/\text{h}$) (Fig. 5b). A well-

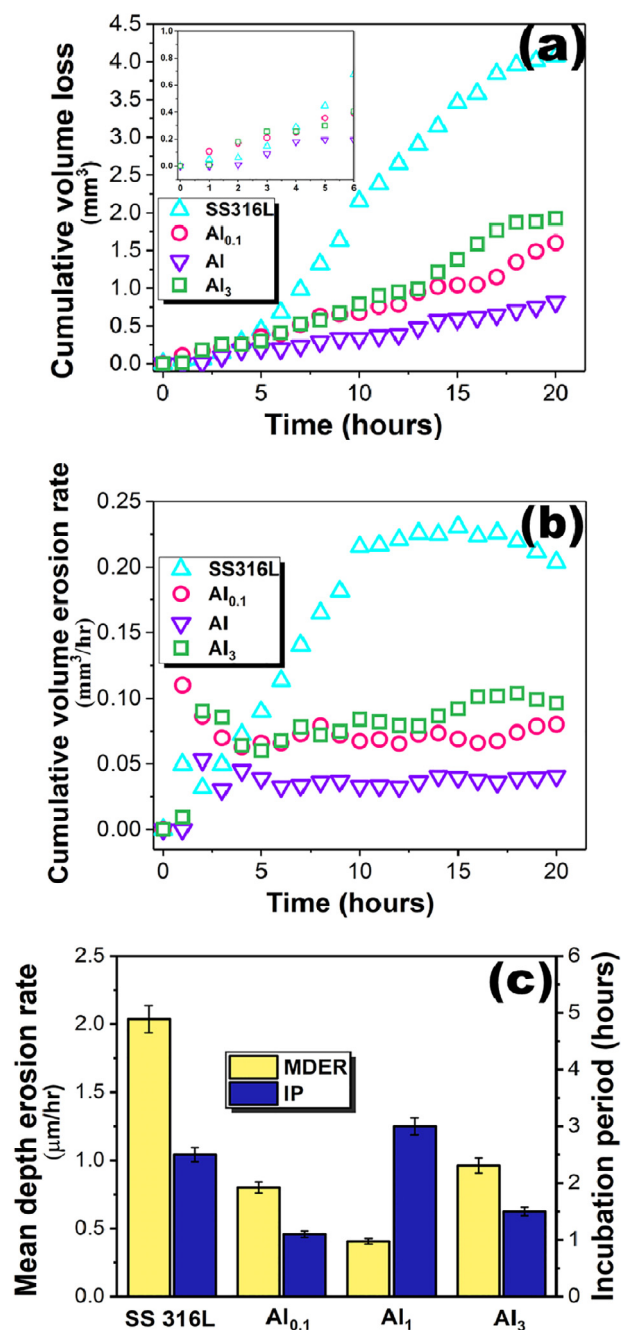


Fig. 7. (a) Cumulative volume loss, (b) cumulative volume rate as a function of exposure time and (c) mean erosion rate and incubation period of Al_{0.1}CoCrFeNi, AlCoCrFeNi and Al₃CoCrFeNi complex concentrated coatings and conventionally used stainless steel 316L subjected to cavitation erosion-corrosion in 3.5% NaCl solution. Inset in (a) shows the magnified view of the initial time duration.

defined deceleration stage was observed for the stainless steel following the maximum erosion rate. Comparatively, the CCA coatings either showed a maximum erosion rate at a very early stage (2.5 h for Al_{0.1}CoCrFeNi compared to 12 h for SS316L steel) or absence of any well-defined maxima, similar to that observed in our prior study conducted on bulk counterpart [7]. The observed behavior might be related with high strain rate sensitivity (\dot{m}) observed for this class of material [36]. Under localized high strain rates produced during cavitation testing, materials with high \dot{m} would promptly strain harden compared to material with low \dot{m} . This can advance the maximum erosion stage resulting in earlier establishment of steady state.

Following, erosion rate maxima, the erosion rates for the coatings stabilized with erosion rate being more or less constant. The steady state erosion rate (\dot{E}_s) observed for Al_{0.1}CoCrFeNi coatings was around 2.4 times higher to that exhibited by the stainless steel. The equimolar and three-molar compositions showed almost similar values of \dot{E}_s and MDER, with AlCoCrFeNi coating exhibiting slightly higher resistance (0.364 μm/h). Further, it is noteworthy that, despite lower hardness (530 HV), the erosion resistance of equimolar CCA was slightly higher/similar to Al₃CoCrFeNi CCA (624 HV). The average erosion rate of former was 13% lower than Al₃CoCrFeNi coating. The erosion resistance of the equimolar coating was also significantly high compared to other conventional compositions possessing extremely high hardness [12,13,37–41]. For in-depth understanding of the degradation resistance, correlation of the cavitation erosion performance of the CCA coatings with different mechanical properties was attempted (Fig. 6). The erosion resistance of the CCA coatings showed good correlation with hardness and strain hardening which explains the better performance of the coatings compared to stainless steel. Hardness showed acceptable correlation (0.84) with \dot{E}_s indicating resistance to plastic deformation being playing an important role (Fig. 6a). High hardness relates to enhanced capability of the material to resist plastic deformation and hence augments cavitation resistance. Higher fraction of B2 phase, solid solution strengthening combined with dislocation pinning by large size Al atom, enhanced the hardness and hence the cavitation erosion resistance for equimolar and Al₃CoCrFeNi coatings. The strain hardening further amplifies the influence of hardness on cavitation behavior (Fig. 6(c)). The CCAs have been observed to exhibit higher strain hardening compared to conventional alloys due to lower stacking fault energy [7,35]. Prior studies suggest that the CCAs exhibit high lattice distortion due to atomic size difference of elements [30,42–44]. The atoms are displaced from their usual lattice positions due to these lattice distortions as a result the energy required for generation and propagation of dislocations will be lower than the conventional materials. This transforms into considerable reduction in the stacking fault energy (SFE) compared to conventional alloys. Mishra et al. [45] reported the addition of Al content increases the lattice distortion resulting in formation of high lattice strain energy. Thus, lower SFE for the CCAs is ascribed to higher lattice strain energy and lower dislocation core energy. Furthermore, our previous studies on bulk Al_{0.1}CoCrFeNi reported higher strain hardening due to lower SFE compared to stainless steel [7,35]. A decrease in stacking fault energy results in widening of partial dislocations which further enhance the work hardening capability [46]. All coatings showed higher strain hardening exponent (n) compared to stainless steel contributing to higher work hardening rate. Further, the presence of large sized atoms such as Al and severe lattice distortion modulates the dislocation motion resulting in higher activation energy. The subsurface hardness of the cavitation erosion tested samples is shown in Fig. 6(d) highlights the contribution of above listed factors towards significant strain hardening. Increase in Al content from 0.1 molar to equimolar resulted in a significant increase in subsurface hardness (~2 times), indicating effective pinning of dislocation line by Al and contribution from Peierls-Nabarro lattice friction contributing towards increased activation energy. However, a further increase in Al fraction to three-molar resulted in a slightly lower subsurface hardness which could be associated with inherently high stacking fault energy (low strain hardening) of Al.

The ratio of hardness to elastic modulus (H/E) which relates with resistance to plastic deformation also showed nominal correlation (Fig. 6(b)). Higher H/E value observed for all the coating indicates enhanced ability to absorb the deformations elastically imposed by repeated implosion of cavitation bubbles. Thus, higher erosion resistance of equimolar CCA coating is attributed to the combined effect of high hardness, increased resistance to plastic deformation, and high work-hardening.

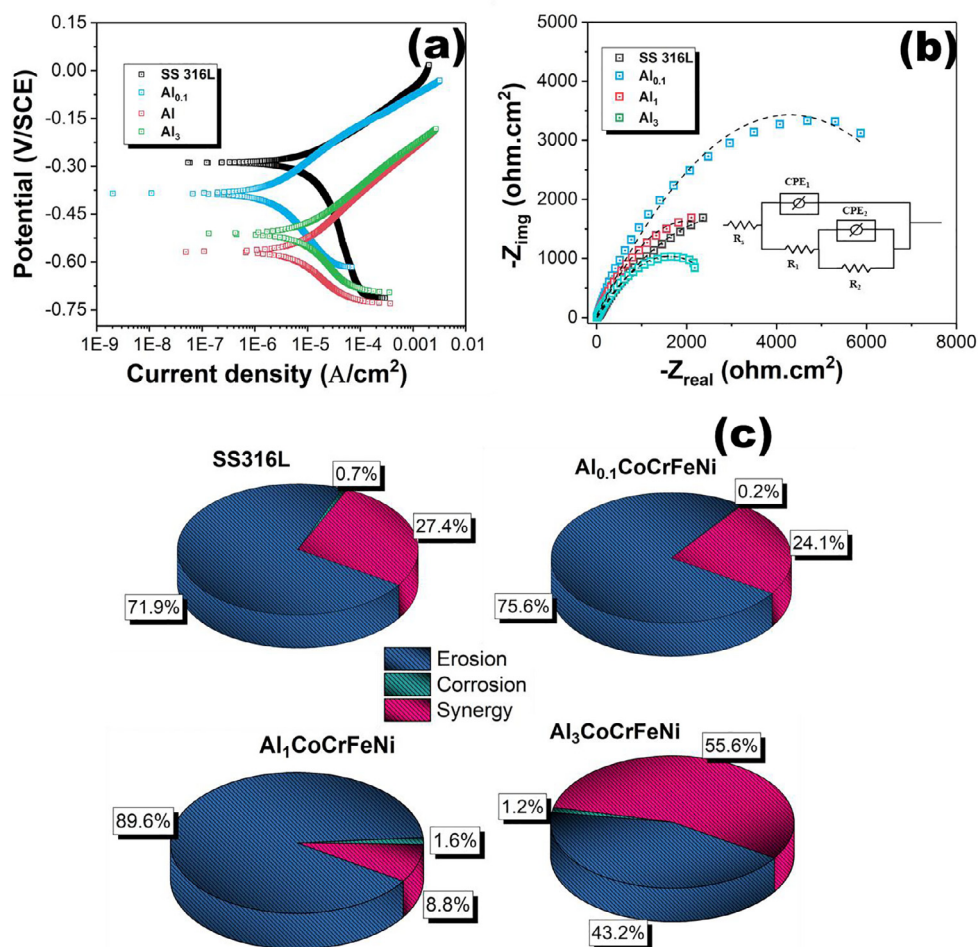


Fig. 8. (a) Tafel and (b) electrochemical impedance test (EIS) for microwave synthesized $\text{Al}_{0.1}\text{CoCrFeNi}$, AlCoCrFeNi and $\text{Al}_3\text{CoCrFeNi}$ complex concentrated coatings with stainless steel using standalone electrochemical corrosion testing and (c) shows the percentage contribution of erosion. Corrosion and synergy calculated for the coatings and steel during cavitation erosion-corrosion testing.

Table 4

The summary of the results obtained using potentiodynamic polarization and electrochemical impedance spectroscopy experiments for the microwave synthesized $\text{Al}_x\text{CoCrFeNi}$ complex concentrated alloys and stainless steel 316L.

Materials	Current density, i_{corr} ($\mu\text{A}/\text{cm}^2$)	Open circuit potential, E_{corr} (mV)	Corrosion rate (mpy)	Polarization resistance, R_p (mV)	Constant phase element exponent (α)
SS316L	11.60 ± 1.6	-289 ± 4.3	4.65 ± 0.093	5.49 ± 0.08	0.71 ± 0.01
$\text{Al}_{0.1}$	1.74 ± 0.013	-385 ± 6.5	0.615 ± 0.001	8.85 ± 0.17	0.83 ± 0.01
Al	5.64 ± 0.075	-568 ± 9.6	2.26 ± 0.004	5.56 ± 0.08	0.72 ± 0.01
Al_3	10.30 ± 1.23	-511 ± 8.6	4.074 ± 0.08	3.01 ± 0.06	0.67 ± 0.01

3.4. Ultrasonic cavitation erosion-corrosion studies

Fig. 7(a) and (b) shows the CVL and CVR for the CCA coatings and the stainless steel subjected to erosion-corrosion testing using 3.5% NaCl solution. As expected, CVL and CVR for all the test samples under erosion-corrosion condition were higher compared to pure erosion condition (Fig. 5(a)). The IP for the equimolar coating was highest among the tested samples with around two to three times (depending upon composition) lower values compared to non-equimolar coatings (Fig. 7(c)). In comparison with pure erosion condition (Fig. 5(c)), the equimolar coating showed lower incubation period ($\sim 39\%$) when tested in 3.5% NaCl solution. It is interesting to observe that under both conditions (3.5% NaCl and distilled water) equimolar exhibited highest degradation resistance. The MDER of the stainless steel increased from $1.464 \mu\text{m}/\text{h}$ under pure erosion condition to $2.037 \mu\text{m}/\text{h}$ when tested with media containing 3.5% NaCl. Among the coatings, MDER was highest for $\text{Al}_3\text{CoCrFeNi}$ ($0.962 \mu\text{m}/\text{h}$) with 130% increase compared to

pure erosion ($0.417 \mu\text{m}/\text{h}$). Simultaneously, MDER of the equimolar CCA coating increased from $0.365 \mu\text{m}/\text{h}$ to $0.406 \mu\text{m}/\text{h}$ (11% increase), respectively. Compared to pure erosion condition, the degradation of the stainless steel under erosion-corrosion condition continued at a constant maximum CVR. Contrarily, the \dot{E}_s of the CCA coatings was lower than the peak CVR. Further, similar to pure erosion case, the time to attain peak CVR was also lower for the coatings compared to the stainless steel due to high strain rate sensitivity. The lower \dot{E}_s following peak CVR observed for coating possibly indicates presence of a stable and protective passive layer.

Standalone electrochemical corrosion studies were performed for all the samples to apprehend the stability of the passive layers and their contribution to degradation behavior. The anodic-cathodic polarization curves obtained using the Tafel test are shown in Fig. 8(a) with results summarized in Table 4. Coatings showed nominally lower current density (i_{corr}) compared to the stainless steel indicating lower corrosion rates for the former. Among the coatings, 0.1 M Al coating showed

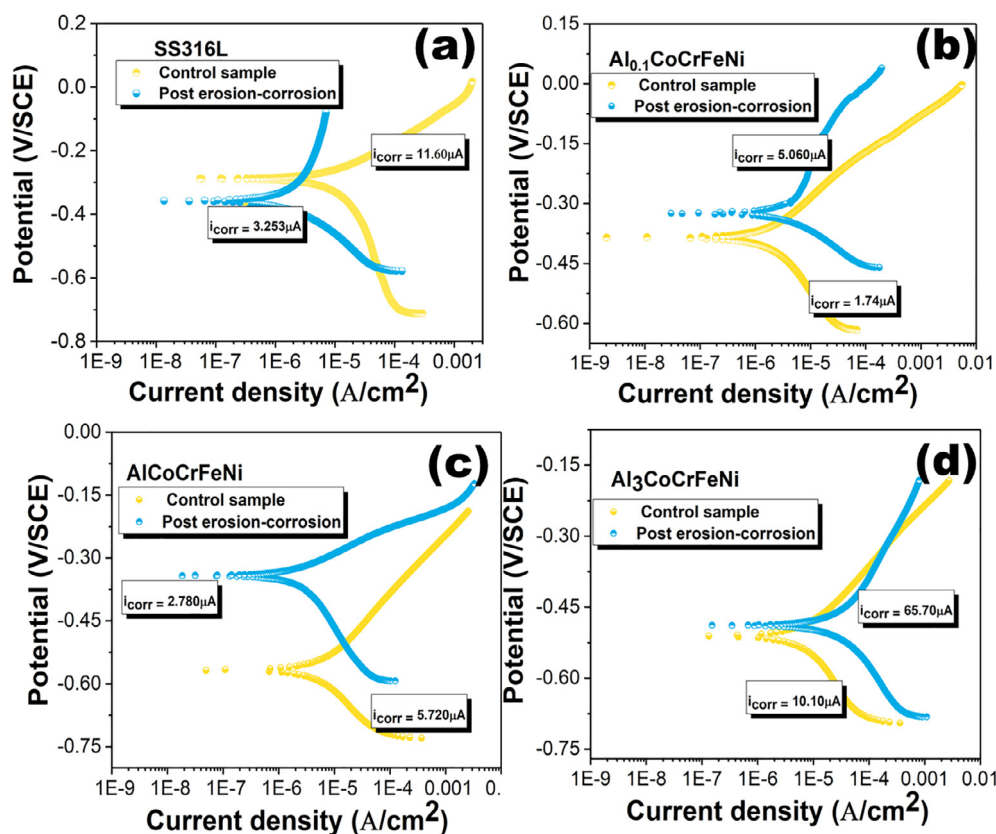


Fig. 9. The potentiodynamic polarization test results of the SS316L stainless steel and microwave synthesized $\text{Al}_x\text{CoCrFeNi}$ complex concentrated coating samples post cavitation erosion-corrosion testing. Control sample represents the test coupon not subjected to cavitation erosion.

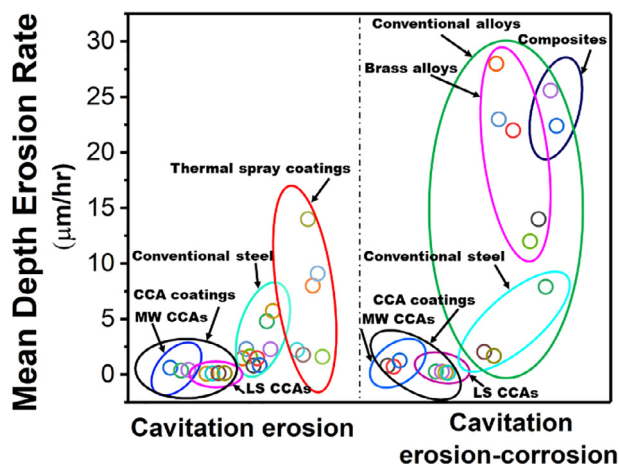


Fig. 10. Comparison of the mean depth erosion rate of microwave derived $\text{Al}_{0.1}\text{CoCrFeNi}$, AlCoCrFeNi and $\text{Al}_3\text{CoCrFeNi}$ complex concentrated coatings with structural materials and conventional coating techniques subjected to erosion and erosion-corrosion conditions [12,13,37–41].

lowest corrosion rates. Higher corrosion resistance of CCAs compared to steel can be mainly attributed to high configurational entropy resulting in sluggish diffusion [35,47]. For coatings, i_{corr} value was observed to increase with higher Al (Fig. 8(a) and Table 4). The $\text{Al}_{0.1}\text{CoCrFeNi}$ coating shows 2.7 times higher i_{corr} in comparison with bulk $\text{Al}_{0.1}\text{CoCrFeNi}$ CCA [7] which is due to the presence of secondary (σ) phase in the former. The formation of σ phase resulted in Cr-depleted intracellular region which deleteriously affected the corrosion resistance. Similar behavior was observed for $\text{Co}_{1.5}\text{CrFeNi}_{1.5}\text{Ti}_{0.5}\text{Mo}_x$ CCAs in NaCl solution [48]. Presence of diffused Mo decreased the corrosion resistance owing to its tendency to promote the formation of

σ phase. Compared to 0.1 molar Al coating, the corrosion rates increased for equimolar (2.266 mpy) and $\text{Al}_3\text{CoCrFeNi}$ (4.074 mpy) coatings despite the absence of σ phase. Similar results were also reported by Shi et al. [10,14]. Higher corrosion rates for these compositions are related with formation of micro galvanic cells due to the presence of B2 phase in intracellular region and higher fraction of Al in the coatings. Higher Al fraction inhibits the formation of Cr oxide film due to lower free energy of Al_2O_3 . The Al_2O_3 passive layer is known to be porous in nature which typically increases the i_{corr} value [10]. The passivation resistance of the passive layers was assessed using electrochemical impedance (EIS) test. The Nyquist plot obtained using EIS is shown in Fig. 8(b). Inset shows the corresponding equivalent electrical circuit (EEC) used for fitting (solid lines) the experimental data (symbols). The obtained values for the different components in EEC are summarized in Table 4. The polarization resistance (R_p) was highest for the $\text{Al}_{0.1}\text{CoCrFeNi}$ coating as also depicted by its largest semi-circle radius. On the other hand, the polarization resistance was lowest for $\text{Al}_3\text{CoCrFeNi}$ with value around two times lower than the stainless steel. The polarization resistance for AlCoCrFeNi coating was twice of that of $\text{Al}_3\text{CoCrFeNi}$. The value of the exponent (α) of the constant phase element (CPE) decreased with an increase in Al fraction in the coatings (Table 4). The value of α was highest for $\text{Al}_{0.1}\text{CoCrFeNi}$ coating compared to all samples indicating the presence of dense passive film. Simultaneously, as indicated by low α value, the passive layer for $\text{Al}_3\text{CoCrFeNi}$ was dispersed. Shi et al. [14] also reported the addition of Al results in a thick and porous passive layer contributing towards higher corrosion rates. Further, the synergistic effect was examined to study the influence of erosion and corrosion on tested samples using Eq. (1)

$$W_S = W_T - W_E + W_C \quad (1)$$

where W_S is the synergy component, W_T is the erosion-corrosion, W_E is

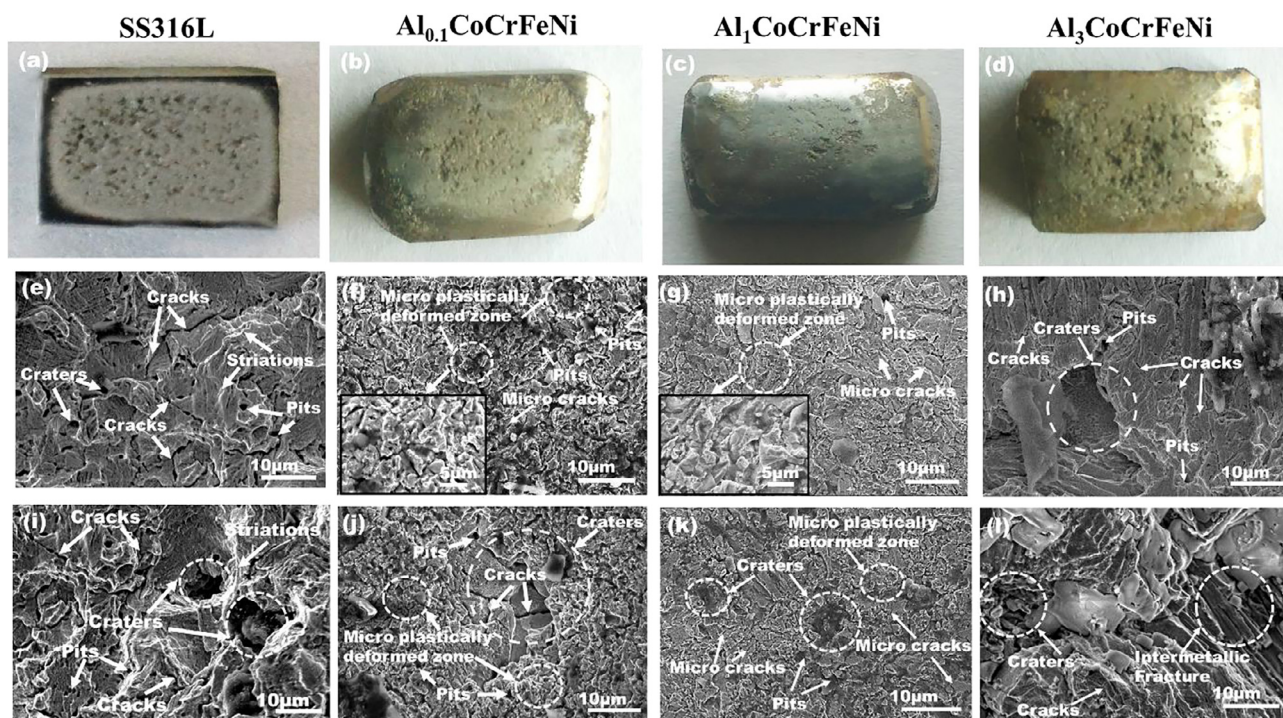


Fig. 11. Macrograph of (a-d) stainless steel and microwave synthesized $\text{Al}_x\text{CoCrFeNi}$ complex concentrated alloy coatings under cavitation erosion-corrosion condition for 20 h. The scanning electron micrograph images showing the surface morphology of the above samples subjected to cavitation (e-h) erosion and (i-l) erosion-corrosion testings. Insets in (f) and (g) show the micron scale TTS fracture of the coating during cavitation exposure.

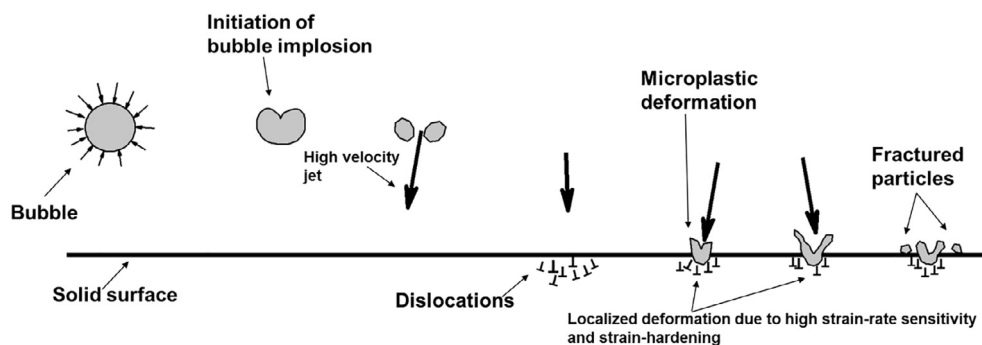


Fig. 12. Schematic illustrating the initiation of tearing topography surface (TTS) failure mode through microplastic deformation during cavitation erosion process for the complex concentrated alloys with high strain-rate sensitivity and strain hardening.

the pure erosion, and W_C is the corrosion under static conditions. Lower synergy was observed for equimolar coating compared to all samples indicating the stability of passive layer under degradation conditions (Fig. 8c). Further addition of Al content (three molar coating) exaggerates the synergy due to the presence of a porous passive layer, which could be easily fractured and removed by impacts of high velocity micro-jets and shockwaves. Presence of such porous passive layer, essentially with low toughness would substantially be detrimental under erosion-corrosion conditions.

For further insight, potentiodynamic polarization testing of the samples post erosion-corrosion was conducted (Fig. 9). Post erosion-corrosion testing all samples showed more noble behavior with maximum effect observed for the equimolar composition and least for the three-molar counterpart. This indicates existence of a stable and protective passive layer for the equimolar composition. Significant change in the i_{corr} values of the all samples was observed. Except equimolar composition, all samples showed increase in i_{corr} values which essentially is related with increased surface area due to pitting, high plastic deformation and presence of disrupted passive layers formed during erosion-corrosion testing. Compared to more than six times higher i_{corr}

value observed for $\text{Al}_3\text{CoCrFeNi}$, a decrease in i_{corr} value of more than two-folds was observed for the equimolar coating, indicating superior passive layer stability of the former. The higher CVR under erosion-corrosion condition for $\text{Al}_3\text{CoCrFeNi}$ is associated with the removal of the weak porous passive layer. High energy jets originating from the implosion of vapor bubbles can easily remove the weak and less stable passive layer resulting in higher erosion-corrosion rate. On contrary, optimum combination of high work hardening, and hardness and good corrosion resistance supplemented by enhanced stability contributed to higher erosion-corrosion resistance for equimolar coating compared to pure erosion. The degradation resistance of the CCA coatings was significantly higher than conventional coatings (Fig. 10) [12,13,37–41]. Furthermore, the degradation resistance of the CCA coatings synthesized using microwave technique was comparable to those obtained using laser cladding process.

3.5. Material removal mechanism

Fig. 11 illustrates the morphology of the test samples subjected to pure erosion and erosion-corrosion conditions. Pronounced level of

macro pits was observed on the stainless steel sample compared to coated samples (Fig. 11(a) to (d)). Among all coatings, $\text{Al}_3\text{CoCrFeNi}$ exhibited highest damage while $\text{Al}_{0.1}\text{CoCrFeNi}$ and equimolar coatings showed moderate level of macro pits (Fig. 11(b) and (c)). Similar level of degradation can also be observed at microscopic scale. Significant number of pits, micro cracks and striations were observed for the stainless steel indicating fatigue controlled plastic deformation (Fig. 11(e)). Compared to stainless steel, the size of both pits and cracks was significantly lowered for the coatings. Coating also showed no clear signs of striations as observed in case of steel. Instead, combined effect of tearing top surface (TTS) mechanism [49] and brittle fracture of intermetallic phases were observed to play a crucial role. TTS is mainly the surface fracture attributed to cyclic fatigue stress at very fine scale. The presence of TTS was more evident for the $\text{Al}_{0.1}\text{CoCrFeNi}$ and AlCoCrFeNi coatings. Contrarily, brittle fracture of the intermetallic phase was observed to more dominant erosion mode for the three-molar composition owing to its lower fracture toughness and high precipitate fraction. The presence of TTS mechanism instead of fatigue striations for the coatings can be associated with their high strain-hardening and strain rate sensitivity inherent to CCAs. The high velocity microjets/shockwaves originating from the collapsing bubbles would induce localized microplastic deformation in form of pits in CCAs (Fig. 12). As a result of high strain-hardening and strain rate sensitivity, the plastic deformation would be restricted to the localized zone as observed in micrographs for the $\text{Al}_{0.1}\text{CoCrFeNi}$ and AlCoCrFeNi CCA coatings. The presence of TTS fracture can also be associated with the presence of secondary interfaces [49]. Morphology of the degraded surface showed almost an insignificant difference with the change in test media (erosion to erosion-corrosion), except brittle fracture of the intermetallic phase was much more evident. The cavities/pits formed during microplastic deformation would act as an active site promoting corrosion and exposing the underlying intermetallic phase.

4. Conclusion

In present work, we developed the $\text{Al}_x\text{CoCrFeNi}$ ($x = 0.1\text{--}3$) complex concentrated alloy coatings using microwave hybrid technique. The coatings were composed of cellular structure with uniform thickness and lower porosity ($< 1\%$). The microstructure of these coatings showed phase transition from FCC ($\text{Al}_{0.1}\text{CoCrFeNi}$) to BCC (AlCoCrFeNi and $\text{Al}_3\text{CoCrFeNi}$) along with the presence of secondary phases (σ and B2) depending upon composition. The difference in microstructures accounted for high hardness with low fracture toughness observed for $\text{Al}_3\text{CoCrFeNi}$ coating and vice-versa for $\text{Al}_{0.1}\text{CoCrFeNi}$ coating. All the coatings showed better cavitation erosion and erosion-corrosion resistance compared to stainless steel. Among the coatings, equimolar composition showed four-times (pure erosion) and three-times (erosion-corrosion) higher degradation resistance compared to stainless steel. The better degradation resistance of the equimolar composition is related with high work-hardening, optimal combination of hardness and fracture toughness and superior corrosion resistance. Presence of porous and unstable passive layer formed for $\text{Al}_3\text{CoCrFeNi}$ coating, as conformed by electrochemical testing on pre and post erosion-corrosion tested samples resulted in their poor resistance. The presence of secondary phases lowered the corrosion resistance of the coatings compared to bulk counterparts which is possibly due to formation of micro galvanic cells and Cr-depletion form the intercellular region. The degradation mechanism for the CCAs was observed to be different from the stainless steels with presence of tearing topography surface (TTS) (except $\text{Al}_3\text{CoCrFeNi}$) been observed to be operational for the former. Compared to pits, cracks and striation, microplastic deformation was the prominent failure mode for the CCAs. The $\text{Al}_3\text{CoCrFeNi}$ showed brittle failure mode with significant fractured intermetallic phases. Equimolar CCA composition was observed to provide highest degradation resistance compared to the non-equimolar counterparts projecting it a potential candidate for fluid machines working under

extreme conditions.

Acknowledgement

H S Grewal thankfully acknowledges the financial assistance provided by Department of Science and Technology (DST) and Science & Engineering Research Board (SERB), India, under project title “Microwave Derived Bi-modular Composite Coatings For Encountering Erosion-Related Problems”, File No. ECR/2015/000106.

Appendix A. Supplementary data

Supplementary data associated with this article can be found, in the online version, at <https://doi.org/10.1016/j.ultsonch.2018.09.004>.

References

- [1] G. Stachowiak, A.W. Batchelor, *Engineering Tribology*, Butterworth-Heinemann, 2013.
- [2] R.J. Wood, *Marine wear and tribocorrosion*, *Wear* 376 (2017) 893–910.
- [3] G. Koch, 1 – Cost of corrosion A2, in: A.M. El-Sherik (Ed.), *Trends in Oil and Gas Corrosion Research and Technologies*, Woodhead Publishing, Boston, 2017, pp. 3–30.
- [4] M.C. Gao, J.-W. Yeh, P.K. Liaw, Y. Zhang, *High-entropy Alloys: Fundamentals and Applications*, Springer, 2016.
- [5] J.W. Yeh, S.K. Chen, S.J. Lin, J.Y. Gan, T.S. Chin, T.T. Shun, C.H. Tsau, S.Y. Chang, Nanostructured high-entropy alloys with multiple principal elements: novel alloy design concepts and outcomes, *Adv. Eng. Mater.* 6 (2004) 299–303.
- [6] B.S. Murty, J.-W. Yeh, S. Ranganathan, *High-entropy Alloys*, Butterworth-Heinemann, 2014.
- [7] R.B. Nair, H. Arora, S. Mukherjee, S. Singh, H. Singh, H. Grewal, Exceptionally high cavitation erosion and corrosion resistance of a high entropy alloy, *Ultrason. Sonochem.* 41 (2018) 252–260.
- [8] W. Kai, C. Li, F. Cheng, K. Chu, R. Huang, L. Tsay, J. Kai, The oxidation behavior of an equimolar FeCoNiCrMn high-entropy alloy at 950 °C in various oxygen-containing atmospheres, *Corros. Sci.* 108 (2016) 209–214.
- [9] I. Moravcik, J. Cizek, P. Gavendova, S. Sheikh, S. Guo, I. Dlouhy, Effect of heat treatment on microstructure and mechanical properties of spark plasma sintered AlCoCrFeNiTi 0.5 high entropy alloy, *Mater. Lett.* 174 (2016) 53–56.
- [10] Y. Shi, B. Yang, X. Xie, J. Brechtel, K.A. Dahmen, P.K. Liaw, Corrosion of Al_xCoCrFeNi high-entropy alloys: Al-content and potential scan-rate dependent pitting behavior, *Corros. Sci.* 119 (2017) 33–45.
- [11] Y. Dong, Y. Lu, J. Kong, J. Zhang, T. Li, Microstructure and mechanical properties of multi-component AlCrFeNiMox high-entropy alloys, *J. Alloy. Compd.* 573 (2013) 96–101.
- [12] S. Zhang, C. Wu, C. Zhang, M. Guan, J. Tan, Laser surface alloying of FeCoCrAlNi high-entropy alloy on 304 stainless steel to enhance corrosion and cavitation erosion resistance, *Opt. Laser Technol.* 84 (2016) 23–31.
- [13] C. Wu, S. Zhang, C. Zhang, H. Zhang, S. Dong, Phase evolution and cavitation erosion-corrosion behavior of FeCoCrAlNiTi_x high entropy alloy coatings on 304 stainless steel by laser surface alloying, *J. Alloy. Compd.* 698 (2017) 761–770.
- [14] Y. Shi, L. Collins, R. Feng, C. Zhang, N. Balke, P.K. Liaw, B. Yang, Homogenization of Al_xCoCrFeNi high-entropy alloys with improved corrosion resistance, *Corros. Sci.* (2018).
- [15] Y. Shi, L. Collins, N. Balke, P.K. Liaw, B. Yang, In-situ electrochemical-AFM study of localized corrosion of Al_xCoCrFeNi high-entropy alloys in chloride solution, *Appl. Surf. Sci.* 439 (2018) 533–544.
- [16] R. Wang, K. Zhang, C. Davies, X. Wu, Evolution of microstructure, mechanical and corrosion properties of AlCoCrFeNi high-entropy alloy prepared by direct laser fabrication, *J. Alloy. Compd.* 694 (2017) 971–981.
- [17] Y.-C.Y. Wei-Lin Hsu, Chia-Yu Chen, Jien-Wei Yeh, Thermal sprayed high-entropy NiCo 0.6 Fe 0.2 Cr 1.5 SiAlTi 0.2 coating with improved mechanical properties and oxidation resistance, *Intermetallics* (2017).
- [18] A.S.M. Ang, C.C. Berndt, M.L. Sesso, A. Anupam, S. Praveen, R.S. Kottada, B. Murty, Plasma-sprayed high entropy alloys: microstructure and properties of AlCoCrFeNi and MnCoCrFeNi, *Metall. Mater. Trans. A* 46 (2015) 791–800.
- [19] H. Zhang, Y. Pan, Y.-Z. He, Synthesis and characterization of FeCoNiCrCu high-entropy alloy coating by laser cladding, *Mater. Des.* 32 (2011) 1910–1915.
- [20] E. Thostenson, T.-W. Chou, *Microwave processing: fundamentals and applications*, *Compos. A Appl. Sci. Manuf.* 30 (1999) 1055–1071.
- [21] D. Gupta, A. Sharma, Development and microstructural characterization of microwave cladding on austenitic stainless steel, *Surf. Coat. Technol.* 205 (2011) 5147–5155.
- [22] R.R. Mishra, A.K. Sharma, Microwave-material interaction phenomena: heating mechanisms, challenges and opportunities in material processing, *Compos. A Appl. Sci. Manuf.* 81 (2016) 78–97.
- [23] E. Colombini, R. Rosa, L. Trombi, M. Zadra, A. Casagrande, P. Veronesi, High entropy alloys obtained by field assisted powder metallurgy route: SPS and microwave heating, *Mater. Chem. Phys.* (2017).
- [24] P. Veronesi, E. Colombini, R. Rosa, C. Leonelli, F. Rosi, Microwave assisted

- synthesis of Si-modified Mn₂₅Fe_xNi₂₅Cu(50–x) high entropy alloys, *Mater. Lett.* 162 (2016) 277–280.
- [25] R.B. Nair, H.S. Arora, P. Mandal, S. Das, H.S. Grewal, High-performance microwave-derived multi-principal element alloy coatings for tribological application, *Adv. Eng. Mater.* 1800163 (2018).
- [26] W.C. Oliver, G.M. Pharr, An improved technique for determining hardness and elastic modulus using load and displacement sensing indentation experiments, *J. Mater. Res.* 7 (1992) 1564–1583.
- [27] C.B. Ponton, R.D. Rawlings, Vickers indentation fracture toughness test Part 1 Review of literature and formulation of standardised indentation toughness equations, *Mater. Sci. Technol.* 5 (1989) 865–872.
- [28] ASTM G32-16, Standard Test Method for Cavitation Erosion Using Vibratory Apparatus, ASTM International, West Conshohocken, PA, 2016, (2016).
- [29] C.-Y. Hsu, C.-C. Juan, T.-S. Sheu, S.-K. Chen, J.-W. Yeh, Effect of aluminum content on microstructure and mechanical properties of Al_xCoCrFeMo_{0.5}Ni high-entropy alloys, *JOM* 65 (2013) 1840–1847.
- [30] W.-R. Wang, W.-L. Wang, S.-C. Wang, Y.-C. Tsai, C.-H. Lai, J.-W. Yeh, Effects of Al addition on the microstructure and mechanical property of Al_xCoCrFeNi high-entropy alloys, *Intermetallics* 26 (2012) 44–51.
- [31] J. Zhu, H. Fu, H. Zhang, A. Wang, H. Li, Z. Hu, Microstructures and compressive properties of multicomponent AlCoCrFeNiMox alloys, *Mater. Sci. Eng., A* 527 (2010) 6975–6979.
- [32] C.-Y. Hsu, C.-C. Juan, T.-S. Sheu, S.-K. Chen, J.-W. Yeh, Effect of aluminum content on microstructure and mechanical properties of Al_xCoCrFeMo_{0.5}Ni high-entropy alloys, *JOM* 65 (2013) 1840–1847.
- [33] H. Zhang, Y. He, Y. Pan, Enhanced hardness and fracture toughness of the laser-solidified FeCoNiCrCuTiMoAlSiB 0.5 high-entropy alloy by martensite strengthening, *Scr. Mater.* 69 (2013) 342–345.
- [34] A. Giannakopoulos, S. Suresh, Determination of elastoplastic properties by instrumented sharp indentation, *Scr. Mater.* 40 (1999) 1191–1198.
- [35] R.B. Nair, H.S. Arora, A. Ayyagari, S. Mukherjee, H.S. Grewal, High entropy alloys: prospective materials for tribo-corrosion applications, *Adv. Eng. Mater.* 1700946 (2018).
- [36] M. Komarasamy, N. Kumar, R.S. Mishra, P.K. Liaw, Anomalies in the deformation mechanism and kinetics of coarse-grained high entropy alloy, *Mater. Sci. Eng., A* 654 (2016) 256–263.
- [37] J. Santa, L. Espitia, J. Blanco, S. Romo, A. Toro, Slurry and cavitation erosion resistance of thermal spray coatings, *Wear* 267 (2009) 160–167.
- [38] M.D.V. Cuppari, R. Souza, A. Sinatora, Effect of hard second phase on cavitation erosion of Fe–Cr–Ni–C alloys, *Wear* 258 (2005) 596–603.
- [39] G. Jiang, Y. Zheng, Y. Yang, H. Fang, Cavitation erosion of bainitic steel, *Wear* 158 (1998) 46–53.
- [40] A. Sakamoto, H. Funaki, M. Matsumura, Influence of galvanic macro-cell corrosion on the cavitation erosion durability assessment of metallic materials—International cavitation erosion test of Gdańsk, *Wear* 186 (1995) 542–547.
- [41] G. Taillon, F. Pougoum, S. Lavigne, L. Ton-That, R. Schulz, E. Bousser, S. Savoie, L. Martinu, J.-E. Klemberg-Sapieha, Cavitation erosion mechanisms in stainless steels and in composite metal–ceramic HVOF coatings, *Wear* 364 (2016) 201–210.
- [42] S. Wang, Atomic structure modeling of multi-principal-element alloys by the principle of maximum entropy, *Entropy* 15 (2013) 5536–5548.
- [43] A. Zaddach, C. Niu, C. Koch, D. Irving, Mechanical properties and stacking fault energies of NiFeCrCoMn high-entropy alloy, *Jom* 65 (2013) 1780–1789.
- [44] Y. Ye, Y. Zhang, Q. He, Y. Zhuang, S. Wang, S. Shi, A. Hu, J. Fan, Y. Yang, Atomic-scale distorted lattice in chemically disordered equimolar complex alloys, *Acta Mater.* 150 (2018) 182–194.
- [45] R. Mishra, N. Kumar, M. Komarasamy, Lattice strain framework for plastic deformation in complex concentrated alloys including high entropy alloys, *Mater. Sci. Technol.* 31 (2015) 1259–1263.
- [46] G.E. Dieter, D.J. Bacon, *Mechanical Metallurgy*, McGraw-hill, New York, 1986.
- [47] H.S. Grewal, R.M. Sanjiv, H.S. Arora, R. Kumar, A. Ayyagari, S. Mukherjee, H. Singh, Activation energy and high temperature oxidation behavior of multi-principal element alloy, *Adv. Eng. Mater.* 19 (2017).
- [48] Y. Chou, J. Yeh, H. Shih, The effect of molybdenum on the corrosion behaviour of the high-entropy alloys Co_{1.5}CrFeNi_{1.5}Ti_{0.5}Mox in aqueous environments, *Corros. Sci.* 52 (2010) 2571–2581.
- [49] A.W. Thompson, J.C. Chesnutt, Identification of a fracture mode: the tearing topography surface, *Metall. Trans. A* 10 (1979) 1193–1196.